

## Two-phase modelling of equiaxed crystal sedimentation and thermomechanic stress development in the sedimented packed bed

This content has been downloaded from IOPscience. Please scroll down to see the full text.

2015 IOP Conf. Ser.: Mater. Sci. Eng. 84 012102

(<http://iopscience.iop.org/1757-899X/84/1/012102>)

View [the table of contents for this issue](#), or go to the [journal homepage](#) for more

Download details:

IP Address: 58.13.7.202

This content was downloaded on 26/06/2015 at 08:23

Please note that [terms and conditions apply](#).

# Two-phase modelling of equiaxed crystal sedimentation and thermomechanic stress development in the sedimented packed bed

A Ludwig<sup>1,\*</sup>, A Vakhrushev<sup>2</sup>, T Holzmann<sup>1</sup>, M Wu<sup>1,2</sup> and A Kharicha<sup>1</sup>

<sup>1</sup> Chair for Modeling and Simulation of Metallurgical Processes, University of Leoben, Austria

<sup>2</sup> Christian-Doppler Laboratory for Advanced Process Simulation of Solidification & Melting, University of Leoben, Austria

\*ludwig@unileoben.ac.at

**Abstract.** During many industrial solidification processes equiaxed crystals form, grow and move. When those crystals are small they are carried by the melt, whereas when getting larger they sediment. As long as the volume fraction of crystals is below the packing limit, they are able to move relatively free. Crystals being backed in a so called packed bed form a semi-solid slurry, which may behave like a visco-plastic material. In addition, cooling-induced density increase of both, liquid and solid phases might lead to shrinkage of the whole casting domain. So deformation happens and gaps between casting and mold occur. In the present work, a two-phase Eulerian-Eulerian volume-averaging model for describing the motion of equiaxed crystals in the melt is combined with a similar two-phase model for describing the dynamic of the packed bed. As constitutive equation for the solid skeleton in the packed bed Norton-Hoff law is applied. Shrinkage induced by density changes in the liquid or the solid phase is explicitly taken into account and handled by remeshing the calculation domain accordantly.

## 1. Introduction

In many practical solidification processes the equiaxed crystals that form first move with the melt when they are small and then sink down and sediment when they are getting larger. Specially, in big steel ingots or in grain refined Al-alloy slabs, large regions usually form by growth and sedimentation of equiaxed crystals. While the melt cools and crystals occur, liquid and solid densities changes with temperature. In addition, often there exist a density change between solid and liquid. For shape and ingot casting or even continuous casting, temperature and phase changed-induced density changes leads to massive shape deformations including the formation of shrinkage cavities and/or microporosity. In last decades, numerical simulation of nucleation, growth, motion and sedimentation of equiaxed crystals have made huge progress especially by means of multi-phase volume averaging methods [1-3]. Also, the simulation of deformation and stresses caused by uneven cooling from solidus to room temperature is a standard procedure today. However, the simulation of flow related phenomena on one side combined with stress and deformation which evolve already during solidification deep inside the mushy zone on the other side is still missing. This paper is supposed to do first steps to close this gap.



In the chemical industry a stack of small objects in a vessel is called packed bed. Much knowledge about permeability of dendritic mushy regions are gained from flow experiments with packed beds. Also the rheological behavior of packed beds made of porous metallic materials saturated with liquid at high temperatures were subject of investigations. Nguyen et al. found for Sn-Pb alloys in the semi-solid state that two functions are needed to describe the corresponding viscoplastic potential [4]. Bellet et al. [5,6] used this viscoplastic potential for the volume-averaged version of the effective macroscopic stress tensor of the solid phase in the mushy zone of a continuous casting of steel. In the present paper, we suggest to combine this approach with a two-phase Eulerian-Eulerian model for motion and sedimentation of equiaxed crystals and a method to deform the mesh in order to account for temperature-induced density changes.

## 2. Model description

### 2.1 Basic considerations

Based on former work of the authors [1-3], a two-phase Eulerian-Eulerian model for simulating formation and sedimentation of equiaxed crystals has been adopted and combined with the two-phase thermomechanic model suggested by Bellet et al [5-6]. The following main considerations were made:

Two phases are defined: the liquid phase ( $\ell$ ) and the solid ( $s$ ). The corresponding phase fractions,  $g_\ell$  and  $g_s$ , add up to one. A predefined number density of already existing grains was considered. The implementation of nucleation and growth of equiaxed crystals is under construction and will be topic of a subsequent paper. Mass-, momentum and enthalpy conservation is solved for both phases by considering (i) above the packing limit a submerged object drag law [6] and an effective solid viscosity which ensures the proper mixture behavior (Eq. (6),(8),(9)), and (ii) below the packing limit a Darcy term drag law with a Kozeny-Carman type permeability and a viscoplastic materials law for the packed bed (Eq. (6),(10)). Note that following the arguments in [6-7], the pressure equilibrium in the liquid phase is almost instantaneous. Subsequently, the interfacial pressures [8] in both phases equal the intrinsic average value of liquid pressure, i.e. its microscopic value.

We also allow that the density of the liquid and solid may vary with temperature. Thus, we have considered corresponding thermal strain rates according to [9]. For the packed bed regime, we use a volume-averaged Norton-Hoff law. As stated in [10], for metallic alloys at elevated temperature the constitution of the solid phase can be characterized by the Norton-Hoff law. According to [5-6] volume-averaging of this law gives a compressible viscoplastic constitutive model which tends to the incompressible viscoplastic Norton-Hoff model as solidification completes (Eq. (10)). As viscoplastic consistency,  $K_v$ , and strain rate sensitivity coefficient,  $m$ , we temperature-averaged the information given in [11] for the low carbon steel (with a composition in mass pct. of 0.06C, 0.1Ni, 0.13Mn, 0.1Si, 0.08Cu, 0.035Al, 0.015P, and 0.012S) and got  $m = 0.139$ . In the current studies we were not satisfied with the  $K_v$  value based on [11], predicting rather low effective viscosity at the viscoplastic regime. To derive the value of  $K_v$ , the assumption of the equality of viscous stress prefactors in Newtonian regime (Eq. (9)) and in viscoplastic one (Eq. (10)) at the coherence limit was made. By ignoring the strain rate influence (assuming  $m = 1$ ) at the transition point, one can derive  $2\mu_s = 3K_v/(g_s A)$ . From this algebraic calculation, we got  $K_v = 7668$  at  $g_s = g_{s,pack} \approx 0.637$ . Please note that the transition point is somehow arbitrary. With a transition at  $g_s = 0.55$   $K_v$  would have been much smaller and so the apparent viscosity of the viscoplastic semi-solid mush. It will be subject of future work to adapt the transition point to a suitable experimental measured  $K_v$ .

**Table 1.** List of equations solved on a grid with moving boundaries. Symbols are defined in the Nomenclature at the end of this paper.

mass conservation	
$\frac{\partial}{\partial t}(g_\ell \rho_\ell) + \nabla \cdot (g_\ell \rho_\ell \mathbf{v}_\ell) = 0$	(1)
$\frac{\partial}{\partial t}(g_s \rho_s) + \nabla \cdot (g_s \rho_s \mathbf{v}_s) = 0$	(2)
momentum conservation	
$\frac{\partial}{\partial t}(g_\ell \rho_\ell \mathbf{v}_\ell) + \nabla \cdot (g_\ell \rho_\ell \mathbf{v}_\ell \mathbf{v}_\ell) = \nabla \cdot g_\ell \boldsymbol{\sigma}_\ell + g_\ell \rho_\ell \mathbf{g} - K_{\ell s}(\mathbf{v}_\ell - \mathbf{v}_s)$	(3)
$\frac{\partial}{\partial t}(g_s \rho_s \mathbf{v}_s) + \nabla \cdot (g_s \rho_s \mathbf{v}_s \mathbf{v}_s) = \nabla \cdot g_s \boldsymbol{\sigma}_s + g_s \rho_s \mathbf{g} + K_{\ell s}(\mathbf{v}_\ell - \mathbf{v}_s)$	(4)
$K_{\ell s} = 18g_\ell^2 \frac{\mu_\ell g_s C_\varepsilon}{d^2} \quad \text{for } g_s < g_{s,pack} \quad \text{with } C_\varepsilon = 10 \frac{g_s}{g_\ell^3}$	(6)
$= g_\ell^2 \frac{\mu_l}{K} \quad \text{for } g_s \geq g_{s,pack} \quad \text{with } K = d \Big _{g_s=g_{s,pack}}^2 \frac{1}{180} \frac{g_\ell^3}{g_s^2}$	
$\boldsymbol{\sigma}_\ell = -p_\ell \mathbf{I} + \boldsymbol{\tau}_\ell, \quad \boldsymbol{\tau}_\ell = 2\mu_\ell (\dot{\boldsymbol{\varepsilon}}_\ell - \frac{1}{3} \text{tr}(\dot{\boldsymbol{\varepsilon}}_\ell) \mathbf{I}), \quad \dot{\boldsymbol{\varepsilon}}_\ell = \frac{1}{2} (\nabla \mathbf{v}_\ell + (\nabla \mathbf{v}_\ell)^T), \quad \text{tr}(\dot{\boldsymbol{\varepsilon}}_\ell) = \nabla \cdot \mathbf{v}_\ell$	(7)
for $g_s < g_{s,pack}$ :	
$\boldsymbol{\sigma}_s = -p_s \mathbf{I} + \boldsymbol{\tau}_s, \quad \boldsymbol{\tau}_s = 2\mu_s (\dot{\boldsymbol{\varepsilon}}_s - \frac{1}{3} \text{tr}(\dot{\boldsymbol{\varepsilon}}_s) \mathbf{I}), \quad \dot{\boldsymbol{\varepsilon}}_s = \frac{1}{2} (\nabla \mathbf{v}_s + (\nabla \mathbf{v}_s)^T), \quad \text{tr}(\dot{\boldsymbol{\varepsilon}}_s) = \nabla \cdot \mathbf{v}_s$	(8)
with $\mu_s = \frac{\mu_l}{g_s} \left( \left( 1 - \frac{g_s}{g_{s,pack}} \right)^{-2.5 g_{s,pack}} - (1 - g_s) \right)$	(9)
for $g_s \geq g_{s,pack}$ :	
$g_s \boldsymbol{\sigma}_s = 3K_v (\sqrt{3} \dot{\boldsymbol{\varepsilon}}_{eq}^s)^{m-1} \left( \frac{1}{A} \dot{\boldsymbol{\varepsilon}}_s - \left( \frac{1}{A} - \frac{1}{3B} \right) \frac{1}{3} \text{tr}(\dot{\boldsymbol{\varepsilon}}_s) \mathbf{I} \right)$	(10)
with $\dot{\boldsymbol{\varepsilon}}_{eq}^s = \frac{1}{A} \sum_{i,j} \dot{\boldsymbol{\varepsilon}}_{s,ij} \dot{\boldsymbol{\varepsilon}}_{s,ij} - \left( \frac{3}{A} - \frac{1}{B} \right) \left( \frac{1}{3} \text{tr}(\dot{\boldsymbol{\varepsilon}}_s) \right)^2$ and defining $\eta_s^{app} = \frac{3K_v}{g_s \rho_s A} (\sqrt{3} \dot{\boldsymbol{\varepsilon}}_{eq}^s)^{m-1}$	
enthalpy conservation	
$\frac{\partial}{\partial t}(g_\ell \rho_\ell h_\ell) + \nabla \cdot (g_\ell \rho_\ell \mathbf{v}_\ell h_\ell) = \nabla \cdot (g_\ell k_\ell \nabla T_\ell) + H^* (T_\ell - T_s)$	(11)
$\frac{\partial}{\partial t}(g_s \rho_s h_s) + \nabla \cdot (g_s \rho_s \mathbf{v}_s h_s) = \nabla \cdot (g_s k_s \nabla T_s) - H^* (T_\ell - T_s)$	(12)
$h_\ell = \int_{T_{ref}}^{T_\ell} c_{p(\ell)} dT + h_\ell^{ref} \quad \text{and} \quad h_s = \int_{T_{ref}}^{T_s} c_{p(s)} dT + h_s^{ref} \quad \text{and} \quad H^* = 10^8 \text{ W/m}^3/\text{K}$	(13)
grain number density conservation and average grain diameter	
$\frac{\partial}{\partial t}(n_s) + \nabla \cdot (n_s \mathbf{v}_s) = 0$	(14)
$d = 2 \cdot \sqrt[3]{\frac{3}{4\pi} \frac{g_s}{n_s}}$	(15)

The two rheological functions  $A(g_s)$  and  $B(g_s)$  used in Eq. (10) are valid for an equiaxed dendritic network (backed bed) and were taken from [4] and reprinted in Table 2. They satisfy  $A(1) = 3/2$  and  $B(1) = 0$ , imposing in that way the incompressibility constraint by means of a penalty factor, the multiplier of  $\dot{\epsilon}_s^{th}$  in Eq. (10), which becomes infinite. Thus, the second term of Eq. (10) vanishes and the equations turns into the regular Norton-Hoff law. Numerically, the penalty factor is made arbitrarily high but finite by replacing  $B(1)$  by  $B(0.999)$ . As coherency limit we have chosen  $g_{s,cohe} = g_{s,pack}$ . All equations solved are gathered in Table 1.

## 2.2. Numerical implementation

The numerical results are obtained by performing the two phase simulation using the in-house multiphase solver developed in the open-source CFD package OpenFOAM®. The heat transfer is included to track the domain shrinkage due to the temperature dependent density change applying the numerical grid motion / smoothing technique.

**Table 2.** Rheological function  $A(g_s)$  and  $B(g_s)$  according to Table 1 in [4]

$$A(g_s) = \frac{3}{2 \cdot g_s^{6.47}} \quad \text{for } g_s > g_{s,cohe} \quad (16)$$

$$B(g_s) = 0.009 \cdot \left[ \frac{1}{g_s^{6.94}} - 1 \right] \quad \text{for } g_s > g_{s,cohe} \quad (17)$$

The mesh motion algorithm is based on the information of the mass fluxes at the domain boundaries required to compensate the volume loss. Therefore a compressible mixture sub-model is applied with the opened domain boundaries as opposed to the closed one for the multiphase model. The boundary displacements are calculated by interpolating the velocity at the face centers to the boundary points. After the boundary points are moved, the internal mesh is smoothed by solving a Laplace equation for the cell centers to maintain the mesh quality [12-14]. This procedure is done for each time step and the coupling between mesh motion and flow calculation is repeated until the zero boundary fluxes are reached.

The presented shrinkage model implementation consists of the following steps:

1. The solution of the multiphase model is obtained for the current iteration.
2. Updated density distribution is calculated.
3. Boundary mass fluxes are calculated from the additional compressible mixture model to compensate the density change, provided from the settling and the heat transfer simulation. Gravity is excluded from the calculations to prevent the liquid / solid mixture run-out.
4. The mesh is moved along the boundaries and sequentially smoothed using a Laplace equation with the provided mesh diffusion coefficient: the bigger coefficient is the more the deformation of the boundaries is smoothed and redistributed through the all mesh elements. Mesh motion fluxes are then included into the convective terms of the multiphase model.
5. The complete multiphase model is recalculated for the next iteration on the modified mesh.
6. Mesh motion / solution updates are continuously repeated until the shrinkage is compensated.
7. The solution is advanced for the next time step.

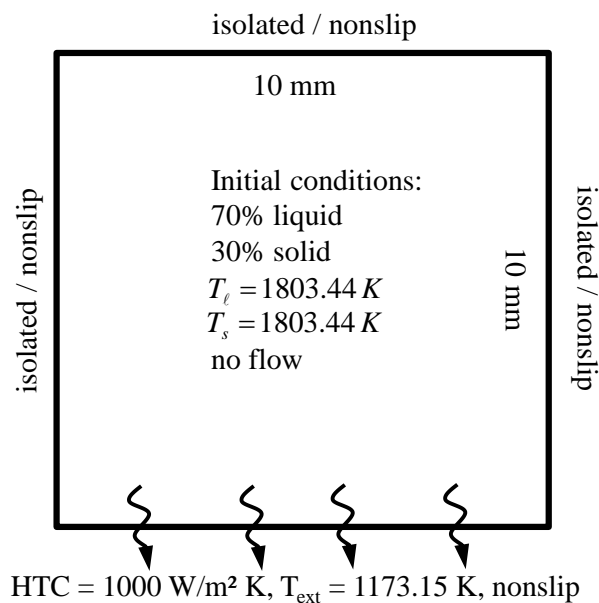


Fig. 1 Domain with the boundary and initial conditions

The simulation domain is shown in Fig. 1 and represents a square cavity (each side is 10 mm), which is isolated from all sides apart of the bottom one. Bottom wall is cooled down with the reference cooling temperature 1173.15 K and the heat transfer coefficient of 1000 W/m<sup>2</sup>K.

The simulations is started with the uniform distribution of the 70% liquid and 30% solid in the whole domain and the initial temperature being uniform for both phases. All walls of the cavity are nonslip and initially we start with a no-flow situation.

**Table 3.** Material properties used in the test case

	$T_{ref}$ , (K)	$c_p$ , (J/kg/K)	$k$ , (W/m K)	$\rho$ , (kg/m <sup>3</sup> )	$\alpha$ , (1/K)	$d$ , (m)
liquid	1803.44	820.6	35.846	7021.95	-	-
solid	1803.44	735.9	35.771	7291	$63 \cdot 10^{-6}$	$10^{-4}$

### 3. Results and discussion

Results of the simulation are shown in Fig. 2, where the evolution of the solid fraction distribution is presented. At the very beginning, both phases obey the Newtonian liquid behavior, and the phase separation interface is quite uniform (see Fig. 2a). Later on the high concentration of the solid above the packing limit (marked with a black line at Fig. 2b) is reached at the bottom of the domain; the apparent (effective) viscosity of the solid phase rapidly increases following the visco-plastic rheology described above. The formation of the coherent solid structures with freckles in between (Fig. 2c) providing the passages for the lighter liquid can be seen. During their development the high solid content zones tend to collapse and to merge together, entrapping some liquid pockets.

The density change for the solid phase is based on the temperature distribution and the compressibility factor  $\alpha$  (see Table 3). One can follow the deformation history of the cavity with time in Fig. 2a-f. It can be noted that (i) the total domain volume is reducing; and (ii) the bottom of the cavity has shrunk more due to the higher concentration of the solid phase, which is the only phase compressing in the presented studies. Please note that all deformations are multiplied by a factor of 2 to make them noticeable on the figures.

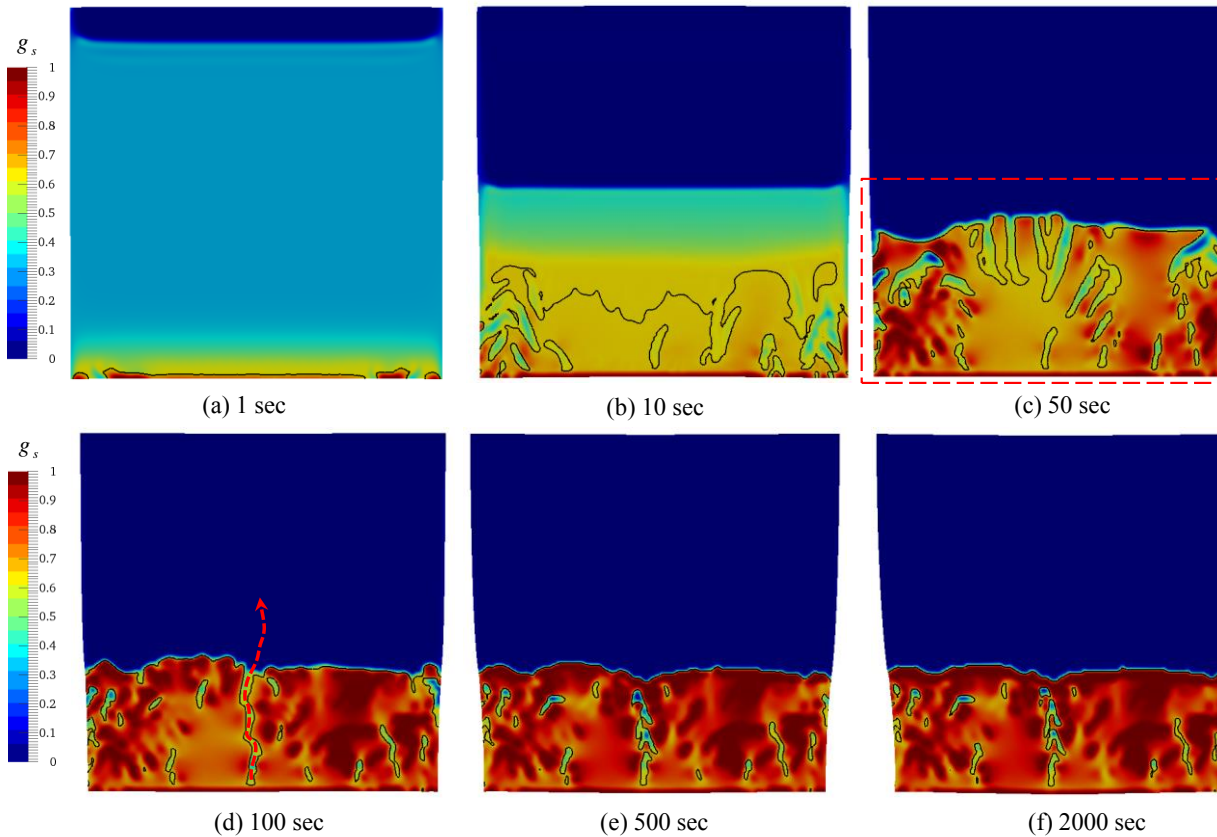


Fig. 2 Evolution of the solid fraction field. The dotted rectangle in (c) is analyzed further in Fig. 3. The arrow in (d) indicated the inner granular melt flow.

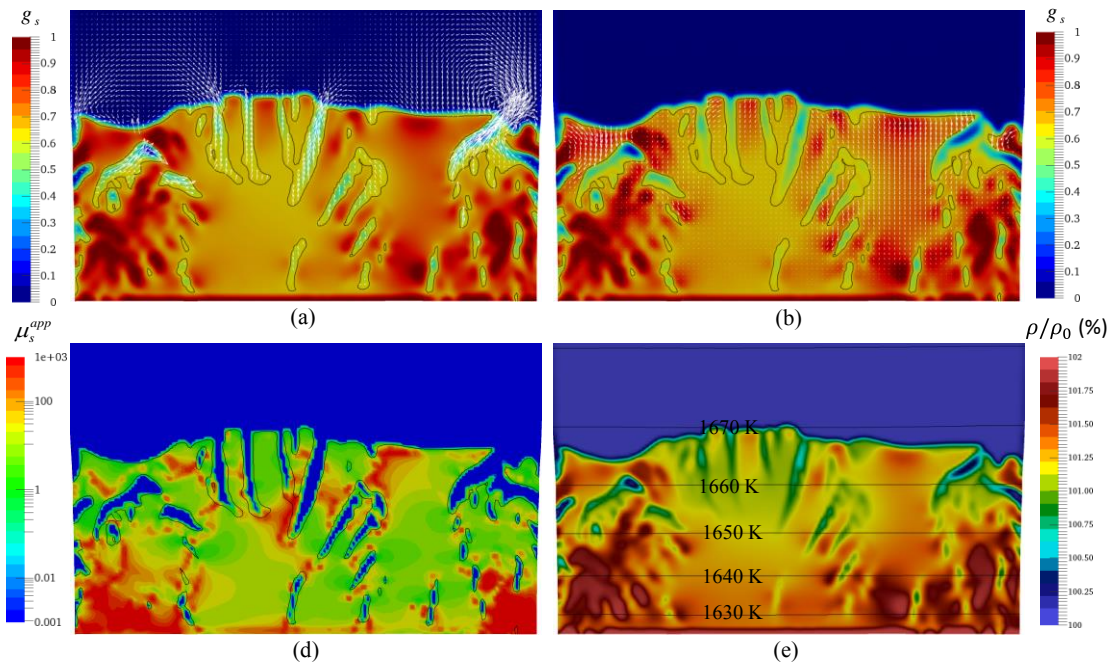


Fig. 3. Results at time  $t = 50$  sec: solid fraction with (a) liquid velocity and (b) solid velocity vectors; (c) apparent kinematic viscosity of the solid  $\mu_s^{app}$  distribution; (d) shrinkage rate: ratio of the calculated mixture density  $\rho(T)$  related to the initial isothermal density  $\rho_0$ ; isotherms show the mixture temperature distribution.

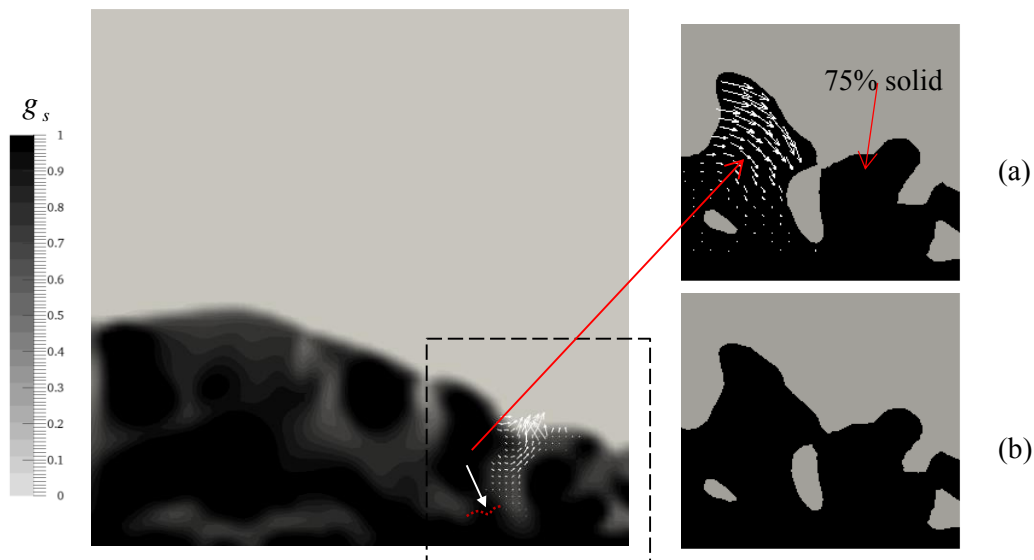


Fig. 4. Collapse of a single solid phase structure: (a) initial moment; solid velocities are shown as vectors; (b) collapsed structure is merged with the more stable one near the cavity wall. The velocity vectors in the large picture shown the liquid velocity escaping from the mush.

With time the initially more or less uniform phase interface becomes quite distorted due to the formation of stable solid (sub-)structures. More over, some zones with higher liquid content (here called liquid pockets) are entrapped between the solid structures.

After the solid phase finally settles at the bottom of the domain, the rest of the liquid floats up through the channels (similar to one marked with a red arrow in Fig. 2d) before they are closed with the coherent solid zones (see Fig. 2e). The stresses occurring in the coherent solid structures are so strong, that they resist any pressure from the uprising liquid, and the rest of it remains entrapped and the final shape of the solid fraction field remains almost unchanged until the system cools down, as shown in Fig. 2e-f.

As it was already mentioned, the heat transfer is simulated together with the solid phase sedimentation causing local density change in the solid phase and the shrinkage of the domain as a consequence of that. Fig. 3 shows the details of the solid / liquid phases interaction at  $t = 50$ sec at the bottom part of the simulation domain, marked with the red dashed rectangle in Fig. 2c. One can see that liquid tends to pass through the freckles / channels in the coherent solid structures, as shown with the vector field in Fig. 3a. Correspondently, the solid phase sinks down and its motion is dominantly downwards (as one can see from Fig. 3b). However, due to the high viscoplastic stresses which appear above the packing limit, the solid velocities are much smaller if compared to the liquid ones (vector scaling is the same in Fig. 3a-b). The distribution of the apparent (effective) viscosity  $\mu_s^{\text{app}}$  of the solid is plotted in Fig. 3d: its maximum value is 6÷9 orders higher than in the liquid, causing a strong resistance to the strain in the dense solid regions. Additionally the shrinkage ratio is presented in Fig. 3e corresponding to the increased density (due to the thermal compression in the domain) to the initial density relation.

Finally, an example of the coherent behavior in the highly packed solid is illustrated as an avalanche / collapsing of the single bound structure (see Fig. 4). The results are taken from an additional simulation not included in the current study. So, if we follow the motion of the marked object, it starts to fall down in the direction of a white arrow in Fig. 4 and to rotate simultaneously, after the small bridge (marked with the red dotted line) collapses under its weight and the liquid escapes from a freckle formed in between coherent solids. In Fig. 4a solid velocities are shown as a vector field indicating that the

bound solid structure moves as a single rotating object, until it impacts by its tip and merges with another more stable one close to the cavity wall.

#### 4. Summary

In order to model both, motion and sedimentation of equiaxed crystals together with stress and deformation in the backed bed, a two-phase Eulerian-Eulerian volume-averaging model is suggested which uses different constitutive models for the stress-strain rate relation of the solid phase below and above the packing limit. In addition, shrinkage induced deformation of the whole domain is accounted for by an adequate remeshing model. As result, the formation of a backed bed of sedimenting equiaxed crystals is models together with the melt flow induced by the sedimentation process. As the solid skeleton is modelled by a visco-plastic flow model, also deformation of and stress evolution in the backed bed is predicted. The results show that the actual dynamic of sedimentation and visco-plastic and density-related deformation might be quite complex as semi-solid channels where liquid can flow more easily might exists in between coherent solid area. The actual dynamic of this process was found to depend highly on the assumed material parameter. As an example, the formation of a continuous crystal pill up and a corresponding initiation of a crystal avalanche / collapsing was shown. The model is the first step towards describing the formation of the solidifying shell together with the occurring gap between mold and metal during thin slab casting of steel.

#### Acknowledgement

This work was financially supported by the FWF Austrian Science Fund (P22614-N22), FFG Bridge Early Stage (No. 3893791), and the Austrian Federal Ministry of Economy, Family and Youth and the National Foundation for Research, Technology and Development within the framework of the Christian Doppler Laboratory for Advanced Process Simulation of Solidification and Melting.

#### Nomenclature

$A, B$	rheological function taken from [4]	$m$	strain rate sensitivity coefficient [-]
$c_{p(\ell)}, c_{p(s)}$	$\ell / s$ specific heat [J/kg/K]	$n_s$	grain number density [-]
$C_\varepsilon$	settling ratio [-]	$p_\ell$	intrinsic pressure in the liquid [kg/s <sup>2</sup> /m]
$d$	vol. averaged grain diameter [m]	$\mathbf{v}_\ell, \mathbf{v}_s$	$\ell / s$ vol. averaged velocity [m/s]
$\mathbf{g}$	gravity acceleration [m/s <sup>2</sup> ]	$T_\ell, T_s$	$\ell / s$ vol. averaged temperature [K]
$g_\ell, g_s$	$\ell / s$ volume fraction [-]	$T_{ref}$	reference temperature [K]
$g_{s,pack}$	packing limit [-]	$\rho_\ell, \rho_s$	$\ell / s$ densities [kg/m <sup>3</sup> ]
$g_{s,cohe}$	coherency limit [-]	$\boldsymbol{\tau}_\ell, \boldsymbol{\tau}_s$	$\ell / s$ vol. av. dev. stress tensor [kg/s <sup>2</sup> /m]
$h_\ell, h_s$	$\ell / s$ volume averaged enthalpy [J]	$\mu_\ell, \mu_s$	$\ell / s$ viscosity [kg/m/s]
$h_\ell^{ref}, h_s^{ref}$	$\ell / s$ enthalpy at $T_{ref}$ [J]	$\mu_s^{app}$	apparent kinematic viscosity of the solid
$\mathbf{I}$	identity tensor [-]	$\alpha$	compressibility [1/K]
$K$	much permeability [m <sup>2</sup> ]		
$K_v$	viscoplastic consistency [kg s <sup>m-2</sup> /m]		
$k_\ell, k_s$	$\ell / s$ eff. heat conductivity [J/m <sup>2</sup> /K]		

#### References

- [1] A Ludwig and M Wu 2002 *Metall. Mater. Trans. A* **33**, 3673-83
- [2] A Ludwig and M Wu 2005 *Mater. Sci. Eng. A* **413-414** 109-14
- [3] M Wu and A Ludwig 2006 *Metall. Mater. Trans. A* **37** 1613-31
- [4] TG Nguyen, D Favier, and M Suery 1994 *Int. J. Plast.* **10** 663-93
- [5] M Bellet 2007 in 9th Int. Conf. Numer. Methods Ind. Form. Process., J.M.A. Cesar de Sa and A.D. Santos, eds., American Institute of Physics, Porto, Portugal, 1369-74

- [6] V Fachinotti, S Le Corre, N Triolet, M Bobadilla and M Bellet 2006 *Int. J. Numer. Methods Eng.* **67** 1341-84
- [7] CY Wang, S Ahuja, C Beckermann, and HC De Groh III 1995 *Metall. Mater. Trans. B* **26** 111-19
- [8] J Ni and C Beckermann 1991 *Metall. Trans. B* **22** 349-61
- [9] M Bellet and BG Thomas 2008 in ASM Handbook, Vol. 15 Cast., ASM International, 449-61
- [10] M Rappaz, M Bellet and M Deville 1998 Numerical Modelling in Materials Science and Engineering, Springer-Verlag, Berlin, Heidelberg, New York
- [11] PF Kozłowski BG Thomas JA Azzi and H Wang 1992 *Metall. Mater. Trans. A* **23** 903-18
- [12] H Jasak, and Ž Tuković 2007 *Trans. FAMENA* **30** 1-18
- [13] H Jasak and Ž Tuković 2010 V Eur. Conf. on Computational Fluid Dynamics 1-6
- [14] T Marić J Höpken K Mooney 2014 *The OpenFOAM Technology Primer* **1** 379-391